PRIMA Metrology

Rider study

Final report

Contract No. 58602/VIF/99/8931/GWI

Doc No. VLT-TRE-IMT-15700-0001.

Technical representative : Samuel Lévêque

Written by: Y. Salvadé email: yves.salvade@imt.unine.ch

A. Courteville email: alain.courteville@imt.unine.ch

Supervised by: R. Dändliker email: rene.dandliker@imt.unine.ch

Address: Institute of Microtechnology
University of Neuchâtel
Rue A.-L. Breguet 2
2000 Neuchâtel
Switzerland

Phone: +41 32 718 3200
Fax: +41 32 718 3201

Date: February 2000

Content

INSTITUT DE MICROTECHNIQUE
UNIVERSITE DE NEUCHATEL

Rue A.-L. Breguet 2
CH - 2000 Neuchâtel, Switzerland
http://www-optics.unine.ch

Phone: +41 32 718 3211
Fax: +41 32 718 3201

PRIMA Metrology
Rider Study

Final report

1 Introduction

The feasibility of the Phase Referenced Imaging and Micro-Arcsecond facility (PRIMA) for the Very Large Telescope Interferometer (VLTI) was recently studied [1, 2, 3]. An interferometric metrology system with high accuracy is required within the framework of PRIMA. The goal of this rider study is to emphasize on specific issues which have been identified in the framework of the PRIMA feasibility study, but could not be tackled in detail because of the limited study time frame.

2 Tasks

The tasks of the work are described in more details in the document “Specifications for the PRIMA Metrology-rider study” [4]. Three specific problems had to be investigated:

- Review and selection of a heterodyne phase detection scheme
- Study of air dispersion correction
- Application of white-light interferometry for internal differential OPD calibration.

3 Technical specifications

The technical specifications are presented in section 5 of the document "Specifications for the PRIMA Metrology-rider study" [4]. The requirements are summarized in the following tables.

Static requirements on optical path	
Max. propagation path (return way)	**Typical value in m**
UT	472
AT	552
Optical path difference (return way)	240

Table 3.1: Optical path lengths to be monitored by the metrology system.

Expected dynamic phase variations (λ = 1 µm) during fringe tracking mode (Telescope pair-wise configuration)	
Sub-system	**Typical value in m**
Delay lines (v = 5 mm/s)	20 kHz
Variable curvature mirror	4 kHz (max.)
Differential delay line (v = 2 µm/s)	8 Hz

Table 3.2: Phase dynamic requirements for the metrology (λ = 1 µm)

Metrology requirements	
Performance	**Value**
Resolution on mean differential OPD	< 0.7 nm
Accuracy on mean differential OPD over 40 msec	< 5 nm
Sampling time (In the case of two independent measurements for each interferometer)	< 4 µsec

Table 3.3: Summary of metrology performance

4 Heterodyne phase detection

4.1 Principle

As required by ESO, we considered two heterodyne interferometers, the first one for the reference object, and the other one for the science object, as shown in Fig. 4.1. The same laser will be used for both interferometers to relax the requirements on the frequency stability of the laser (10^{-8}). A Nd:YAG laser emitting a wavelength of 1064 nm was considered (ν = 300 THz). The frequency shifter module is devoted to generate the heterodyne frequencies by means of acousto-optic modulator (AOM). In order to avoid any crosstalk between the two interferometers, two different frequency shifts f_1 and f_2 are chosen, and a frequency offset $\Delta\nu$ is generated between the two interferometers. We assume therefore that we use the optical frequencies ν and $\nu + f_1$ for the science interferometer, and the frequencies $\nu + \Delta\nu$ and $\nu + \Delta\nu + f_2$ for the reference interferometer. After ac coupling, the two detected interference signals are of the form

$$I_1(t) = I_1 \cos(2\pi f_1 t + \phi_1) \text{ and } I_2(t) = I_2 \cos(2\pi f_2 t + \phi_2), \quad (1)$$

where ϕ_1 and ϕ_2 are the interferometric phases. For arm lengths L_{11} and L_{12} of the science interferometer, the interferometric phase ϕ_1 is

$$\phi_1 = \frac{4\pi(\nu + f_1)}{c} L_{12} - \frac{4\pi\nu}{c} L_{11} = \frac{4\pi\nu}{c} L_1 + \frac{4\pi f_1}{c} L_{12}, \quad (2)$$

where $L_1 = L_{12} - L_{11}$ is the optical path difference of the science interferometer. The last term of Eq. (2) $4\pi f_1 L_{12}/c$ is very few sensitive to the arm length L_{12}. Indeed, assuming f_1 = 500 kHz, a variation of L_{12} of 1 m introduces a phase variation of only $2\pi/300$. Therefore, if the frequency $\nu + f_1$ is injected in the arm which has no active delay line, this term acts as a constant phasor element and has therefore no effect on the incremental metrology. As long as the passive delay line is not moved, this term can be neglected. By applying the same argumentation for the reference interferometer, the interferometric phases can be approximated by

$$\phi_1 = \frac{4\pi\,\nu}{c} L_1 \text{ and } \phi_2 = \frac{4\pi\,(\nu + \Delta\nu)}{c} L_2, \quad (3)$$

where L_1, L_2 are the optical path difference for the science and reference interferometer, respectively. The optical path differences are related to the geometrical path differences by the refractive index of air (see chapter 5).

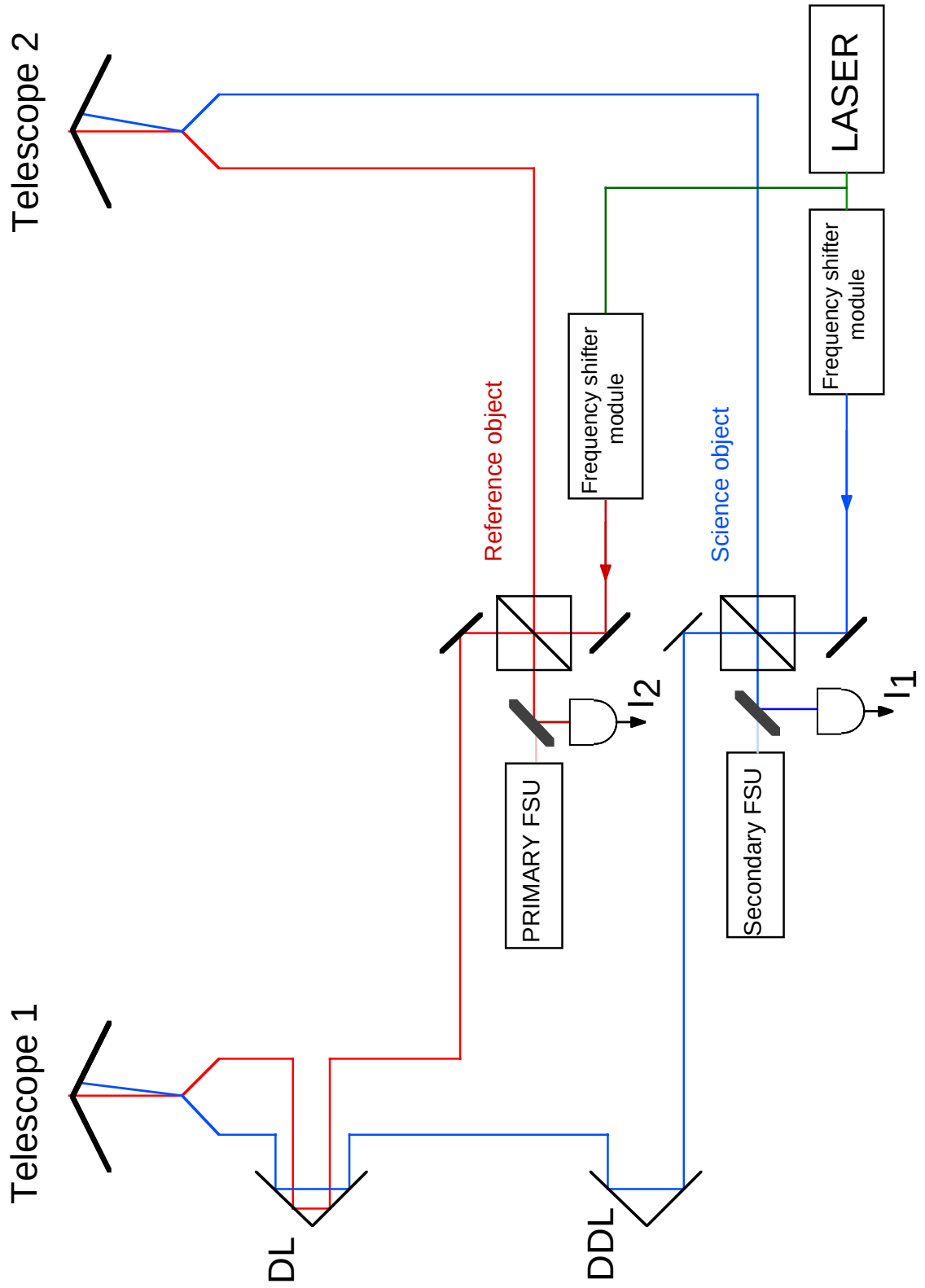

Figure 4.1: Set-up for measuring the differential optical path difference

4.2 Measurement of the differential optical path difference

For the PRIMA facility, the differential optical path difference $\Delta L = L_1 - L_2$ is of interest. Different solutions can be considered to access this value.

4.2.1 Independent measurements for each interferometer

In that case, two independent measurements of ϕ_1 and ϕ_2 are considered. The differential optical path difference is then computed using the relation

$$\Delta L = \phi_1 \frac{c}{4\pi\nu} - \phi_2 \frac{c}{4\pi(\nu + \Delta\nu)}. \tag{4}$$

The two independent measuring systems should be able to monitor the maximal frequency phase variations. This maximal frequency is mainly caused by the maximal tracking speed of the delay line, and is about 25 kHz (see Table 3.2). Simultaneous measurement of ϕ_1 and ϕ_2 is mandatory to obtain the desired accuracy on the differential optical path difference. Indeed, assuming a velocity of the delay line of 5 mm/s, the two measurements should be performed within a time interval of Δt = 5 nm/(2 x 5 mm/s) = 0.5 µs to achieve the desired accuracy (5 nm). This simultaneity requirement may be difficult to obtain depending on the phase measurement technique.

4.2.2 Superheterodyne detection

Superheterodyne detection was initially developed for two-wavelength interferometry [5], and allows to access directly the difference of the interferometric phases related to each wavelength. A similar approach can be used to access directly the phase difference $\phi_1 - \phi_2$. Indeed, by mixing electronically the two interference signals and by band-pass filtering around $f_1 - f_2$, we obtain a signal

$$I_{mes}(t) = I_{12} \cos\left[2\pi(f_1 - f_2)t + \phi_1 - \phi_2\right]. \tag{5}$$

Similarly, we can generate a reference signal of frequency $f_1 - f_2$ from the two individual reference signals related to each interferometer, i.e.

$$I_{ref}(t) = I_{12} \cos\left[2\pi(f_1 - f_2)t\right]. \tag{6}$$

By measuring the phase difference between I_{mes} and I_{ref}, we see that we get direct access to $\phi_1 - \phi_2$. From Eqs. (3), we show that the phase difference is given by

$$\phi_1 - \phi_2 = \frac{4\pi\,\nu}{c}\Delta L - \frac{4\pi\,\Delta\nu}{c} L_2. \tag{7}$$

The first term depends only on the differential optical path difference. However, the second term is sensitive to the individual optical path difference L_2 of the reference interferometer. Since $\Delta\nu$ can be chosen small, the phase difference is not very sensitive to L_2. For $\Delta\nu = 2$ MHz, a variation of L_2 of 1 m introduces a phase variation of only $2\pi/75$. However, since the delay line can move over several meters during the observation, we have to take this phase variation into account. Therefore the variation of the individual OPD δL_2 must be monitored in order to estimate the corresponding phase variation

$$\delta\phi = \frac{4\pi\ \Delta\nu}{c}\delta L_2 . \tag{8}$$

The individual OPD variation δL_2 can be monitored using the individual interference signal $I_2(t)$ and its corresponding reference signal at frequency f_2. Assuming $\Delta\nu$ = 2 MHz, the displacement δL_2 must be measured with an accuracy of only 7 cm to estimate $\delta\phi$ with an accuracy better than $2\pi/1000$. Therefore a simple fringe counter is amply sufficient to measure δL_2 with the desired accuracy. From Eqs. (7) and (8), we see that the differential OPD is given by

$$\Delta L = \frac{c}{4\pi\ \nu}\left(\phi_1 - \phi_2 + \delta\phi\right). \tag{9}$$

Since the maximal velocity of the delay line is limited to 5 mm/s, an update rate for the value $\delta\phi$ of 1 s is fast enough to calculate the differential optical path difference with an accuracy of 5 nm. Indeed, for $\Delta\nu$ = 2 MHz, we see from Eqs. (8) and (9) that the corresponding maximal error on ΔL is only of 5 mm x $\Delta\nu/\nu$= 0.05 nm.

4.2.3 Preferred concept

Superheterodyne detection allows a more direct measurement of the differential optical path difference. In addition, since the phase difference $\phi_1 - \phi_2$ varies much slower than the individual phases, the phase measurement can be performed with a longer integration time by averaging over many cycles (see chapter 4.4). This technique is therefore the most promising for the PRIMA metrology.

The two interference signals for the science and reference interferometers have to be bandpass filtered around f_1 and f_2 respectively to suppress possible cross-talks between each channel. The bandwidth of the filters should be of about 50 kHz (i.e. ± 25 kHz) in order to monitor the maximal tracking speed of the delay line (see Table 3.2). The two heterodyne frequencies must be chosen separated enough to suppress at the most the possible cross-talks. We considered therefore heterodyne frequencies of $f_1 = 650$ kHz and $f_2 = 450$ kHz. Then, the two signals are

mixed by means of analog electronic circuit. After this electronic mixing, an output bandpass filter around $f = f_1 - f_2 = 200$ kHz has to be used to suppress the frequency $f_1 + f_2$, as well as the residual components at f_1, f_2 and DC. The differential delay line is specified to travel a distance of 32.5 mm in 15 s, corresponding to a dynamic phase variation of 9 kHz. A bandwidth of 50 kHz for the output bandpass filter is therefore amply sufficient to monitor the maximal speed of the differential delay line.

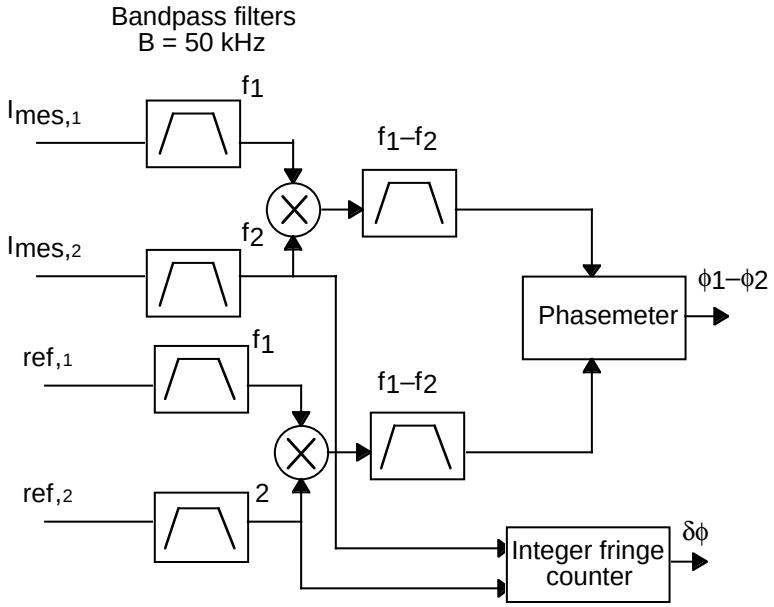

Figure 4.2: Layout of the preferred concept for the measurement phase.

Because of the relatively long observation time, the thermal drift of the filters should be minimized to achieve the desired accuracy. The most critical parameter is the phase shifts introduced by the filters, which may depend on the working temperature. To suppress at the most the thermal drifts, identical filters must be manufactured for the generation of the reference signal $I_{ref}(t)$, and the electronics must be arranged in the same temperature environment. In that way, the phase shift caused by a variation of the ambient temperature can be as low as 0.3 mrad/°C [6].

The preferred concept for the phase measurement is illustrated in Fig. 4.2, including the fringe counter for the monitoring of δL_2.

4.3 Power limitation

Because of the diffraction losses over the large path length, the optical power transmission of the laser metrology beam through the interferometers may be very low (about 1% or even lower). In order to achieve the desired accuracy, the signal-to-noise ratio of the interference signals must be

high enough. The signal-to-noise ratio (SNR) depends on the detected optical power. A minimal power is therefore required on the photodiode to achieve the 5 nm accuracy.

4.3.1 SNR limitation

We consider in this section the example of zero-crossing phase-meter. A well-known limitation for zero-crossing phasemeter is the trigger error. The noise of the signal at the zero-crossing introduces a time uncertainty, as shown in Fig. 4.3.

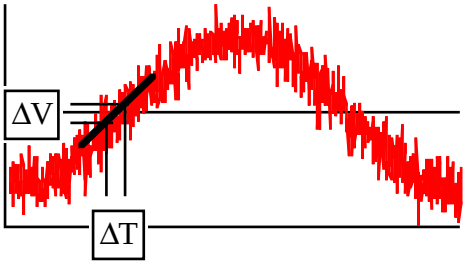

Figure 4.3: Trigger error

The time error Δt depends on the rms amplitude of the noise ΔV_{rms} and on the first derivative of the signal at zero-crossing, i.e.

$$\Delta t = \Delta V_{rms} \Big/ \left.\frac{dV}{dt}\right|_{V=0} . \qquad (10)$$

For a cosine of frequency f and amplitude V (0 to peak), the first derivative at zero-crossing is

$$\left.\frac{dV}{dt}\right|_{V=0} = 2\pi f V . \qquad (11)$$

In zero-crossing phase-meters, the phase is determined by measuring the time interval between the zero-crossing of the reference signal and of the probe signal. Noise on the reference and probe signals introduce time errors Δt_{ref} and Δt_{mes}, respectively. We see that the phase error corresponding to the time errors Δt_{mes} and Δt_{ref} is

$$\delta\phi = 2\pi f \sqrt{\Delta t_{mes}{}^2 + \Delta t_{ref}{}^2} . \qquad (12)$$

In practice, we expect that the reference signal is much less noisy than the probe signal. However, in order to consider the worst case, we assume in the following calculations that both signals introduce the same time error Δt. Using Eqs (10), (11) and (12), we show that

$$\delta\phi = \sqrt{2}\,\frac{\Delta V_{rms}}{V} . \qquad (13)$$

On the other hand, the signal-to-noise ratio of the heterodyne signals is defined as the ratio between the electrical power of the signal and the electrical power of the noise, i.e.

$$SNR = \frac{P_{signal}^{el}}{P_{noise}^{el}} = \frac{V^2 \langle \cos^2(2\pi ft + \phi) \rangle}{\Delta V_{rms}{}^2} = \frac{1}{2} \frac{V^2}{\Delta V_{rms}{}^2}. \quad (14)$$

From Eqs (13) and (14), we see that

$$\delta\phi = \frac{1}{\sqrt{SNR}}. \quad (15)$$

If the noise of the reference signal can be neglected, the phase accuracy will be $\sqrt{2}$ times better. It can be shown that Eq. (15) applies for any type of phase detection. Indeed, the same result can be derived from the phasor representation of a noisy component on a harmonic signal [7].

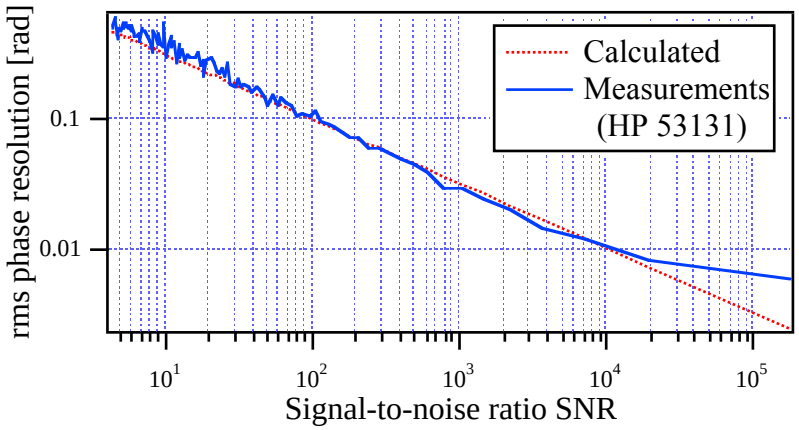

Figure 4.4: Phase accuracy as a function of the signal-to-noise ratio SNR

In order to verify experimentally this relation, we simulated the interference signals by adding electronically a sinusoidal signal and a white noise generated by an arbitrary waveform synthesizer (Stanford Research Systems model# DS 345). Different SNR were obtained by changing the noise level. The phase was measured by means of a universal counter (HP53131) over an integration time of 2 µs. The standard deviation of the phase was estimated from 100 independent phase measurements. Results are shown in Fig. 4.4. We see that the measured values are in good agreement with the values predicted by Eq. (15) for SNR ≤ 10'000 (40 dB). For SNR > 10'000, the phase error is lower than expected because of the input amplifier noise of the counter.

From Fig. 4.4, we show that a SNR of 10'000 is required in order to obtain a phase accuracy better than 10 mrad (2π/600), corresponding to a distance resolution of 0.83 nm.

4.3.2 Noise in photodetection

The noise of the interference signals are generated mainly in the photodetection. A typical detector circuit is depicted in Fig. 4.5. Several sources of noise are inherent in the process of photodetection:

- Shot noise: This is a well-known fundamental limit, which is due to the random fluctuations of the photons which arrive onto the detector. The shot noise is conveniently described by Poisson statistics. The variance of the shot noise is therefore given by the mean number of photo-electrons. It can be shown [8] that the corresponding electrical power is

$$P_{SN} = \frac{2e^2 B \frac{\eta}{h\nu} P_{opt} R^2}{R_L}, \tag{16}$$

  where B is the detection bandwidth, e is the electron charge, η is the quantum efficiency of the detector, and P_{opt} is the mean optical power. In order to simplify the notation, we will use further the spectral sensitivity of the photodiode $S = \eta e/h\nu$.

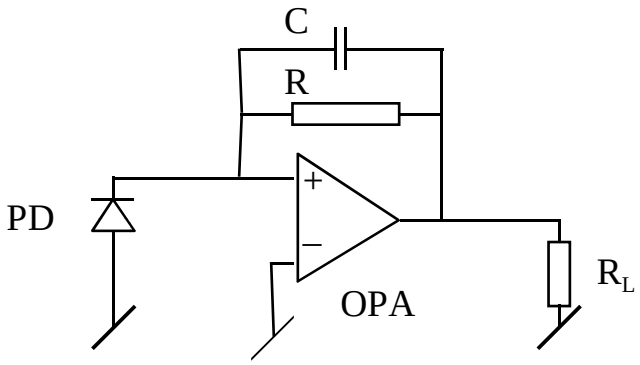

Figure 4.5: Transimpedance circuit. PD: photodiode; OPA: operational amplifier.

- Johnson noise (or thermal noise): The contribution of the thermal noise can be expressed as

$$P_{TN} = 4k_B TB \frac{R}{R_L}, \tag{17}$$

  where k_B is the Boltzmann constant, and T is the temperature.

- Amplifier noise P_{AN}: Depending on the type of amplifier, the contribution of the current noise and the voltage noise at the input of the electronic amplifier cannot be neglected. However, using high-performance amplifiers (e.g. Burr-Brown OPA 627), this contribution can be lower than the thermal noise at T = 300 K.

- Laser intensity noise P_{IN}: Nd:YAG lasers are usually affected by intensity noise. The intensity noise is caused by the intensity fluctuations of the pump laser diode. An active noise reduction allows to reduce substantially this effect. We measured a residual noise of about 0.015% over the range 5 Hz to 500 kHz (approximately white noise) for a Lightwave NPRO Nd:YAG laser.

The dark-current of the photodiode is usually very small compared to the other contribution, and can therefore be neglected. On the other hand, the amplitude of the interference signal is given by $2m\sqrt{P_{opt,1}P_{opt,2}}$, where $P_{opt,1}$ and $P_{opt,2}$ are the optical powers related to each arm of the interferometer, and m is the interference contrast. Assuming the same optical power in each arm, i.e. $P_{opt,1} = P_{opt,2} = P_{opt}/2$, we have

$$P_{ac} = \frac{1}{2} m^2 S^2 P_{opt}{}^2 \frac{R^2}{R_L}, \tag{18}$$

where S is the spectral sensitivity of the photodiode. The SNR is then found to be

$$SNR = \frac{P_{ac}}{P_{SN} + P_{TN} + P_{AN} + P_{IN}}, \tag{19}$$

Numerical simulations were performed using the software MathCad. Experimental results were obtained using a Lightwave Nd:YAG laser, and an InGaAs photodetector (photodiode Hamamatsu G3476-10). The electrical power of the amplifier noise P_{AN} was measured to be 75 pW over 500 kHz (50 Ω load resistance), which is approximately 5 times larger than the thermal noise. As already mentioned, this noise could be substantially reduced by using improved electronic components. The feedback resistance R was of 100 kΩ, and the quantum efficiency of the photodiode was estimated to be about 0.8 (typical value for InGaAs photodiodes at 1064 nm).

From Eqs (16)–(19), we calculated the signal-to-noise ratio as a function of the optical power for a fringe visibility of 80%. On the other hand, we measured the power spectral density of the noise using a FFT analyser over the range 10 kHz to 510 kHz for different optical powers P_{opt},. The ambient temperature T was approximately 300 K. We computed then the corresponding signal-to-noise ratio. Since a cw optical power was used during the measurement, the SNR_{dc} was divided by 2 to estimate the signal-to-noise ratio SNR_{ac} of a modulated signal with amplitude P_{opt}. In addition, the SNR_{ac} is multiplied by 80% in order to simulate the non-ideal fringe contrast. As shown in Fig. 4.6, the measured values correspond very well to the predicted ones.

The amplifier noise is dominant up to 2 µW, and the intensity noise dominates the other sources of noise above 30 µW.

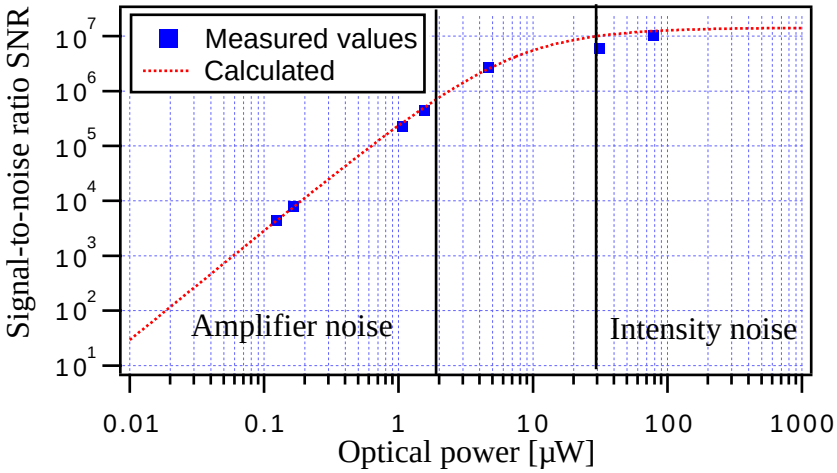

Figure 4.6: SNR as a function of the optical power

4.3.3 Required optical power

From Fig. 4.6, we show that an optical power of 200 nW (i.e. 100 nW in each interferometric arm) is required to achieve a SNR of 10'000, corresponding to a phase accuracy of $2\pi/600$. However, it should be noted that this estimation is made for a detection bandwidth of 500 kHz. As discussed in chapter 4.2.3, the output signal would be band-pass filtered with a bandwidth of 50 kHz. The minimal detectable power is therefore expected to be reduced by a factor $\sqrt{10}$. In addition, the resolution can be improved by averaging the output of the phasemeter, in order to obtain the 5 nm accuracy over T = 40 ms (see Table 3.3). An optical power of 200 nW on the photodetector should be amply sufficient to achieve the desired accuracy, assuming a fringe visibility of 80%.

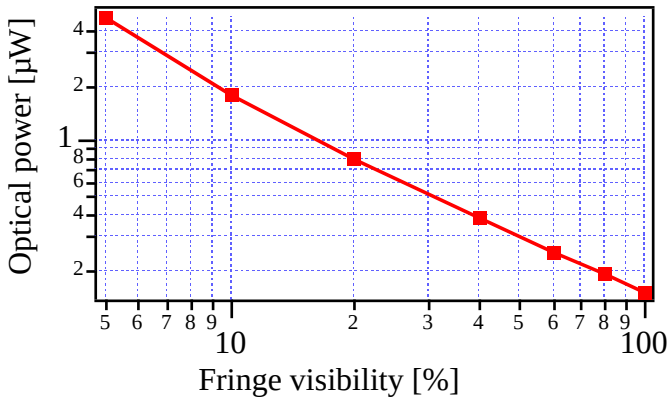

Figure 4.7: Required optical power as a function of the fringe visibility

Lower fringe visibility may be obtained if the wavefronts of the two interfering beams are not adapted. Figure 4.7 shows the minimal optical power for SNR = 10'000 as a function of the fringe visibility (bandwidth of 500 kHz).

4.4 Phase detection technique

The phase measurement unit should consist of an integer fringe counter, which counts the number of λ/2 displacement, and an additional fractional fringe counter.

4.4.1 Integer fringe counter

The principle of the integer fringe counter is shown in Fig. 4.8. It consists simply of an up/down counter, which is incremented by the reference signal and decremented by the probe signal. The value of the counter is then read-out (read signal) immediately after a transition of the probe signal has occurred. The same principle is used in Hewlett-Packard interferometers, but with an additional frequency multiplier before the counter to improve the resolution. Up/down counter chips are commercially available (e.g. National Semiconductor).

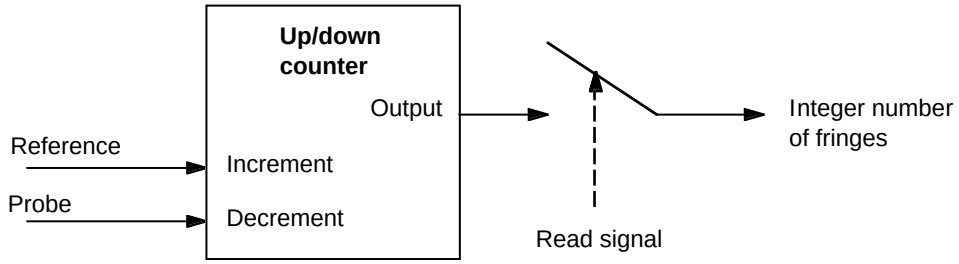

Figure 4.8: Integer fringe counter.

Different types of phasemeter can be used to measure the fractional part of the fringe.

4.4.2 Analog phase demodulator

The typical layout for analog phase demodulation is shown in Fig. 4.9. This type of demodulator was used for instance in former Revox FM tuners. The interference signals are first converted to square signals by means of limiting amplifiers. A mixer (e.g. AND gate) is then used to produce a pulse train whose duration is proportional to the phase difference between the reference and the probe signals. The final low-pass filter is then used to convert the pulse-width to a voltage. One gets therefore a signal which is proportional to the phase difference. For phase jumps from +180° to –180°, the phase measurement will be perturbed. Two signals in quadrature can be generated to solve this problem. For that purpose, the reference signal is phase-shifted by 90°, before the mixing with the probe signal. Figure 4.9 shows the two output signals $U_{out,A}$ and $U_{out,B}$ that would be obtained for a constant speed of the differential delay line.

The cut-off frequency of the low-pass filter has to be much smaller than the heterodyne frequency. A digital version was recently developed at IMT [7], which allows to increase the

frequency response to a few 100 kHz. The principle consists of charging a capacitance as long as the pulse is high; then this voltage is hold and synchronously sampled by an A/D converter. We note however that the slow frequency response of the analog phase demodulator is not a limitation for the selected superheterodyne detection scheme, since the fastest variation of $\phi_1 - \phi_2$ (about 9 kHz) is much smaller than the chosen superheterodyne frequency (200 kHz).

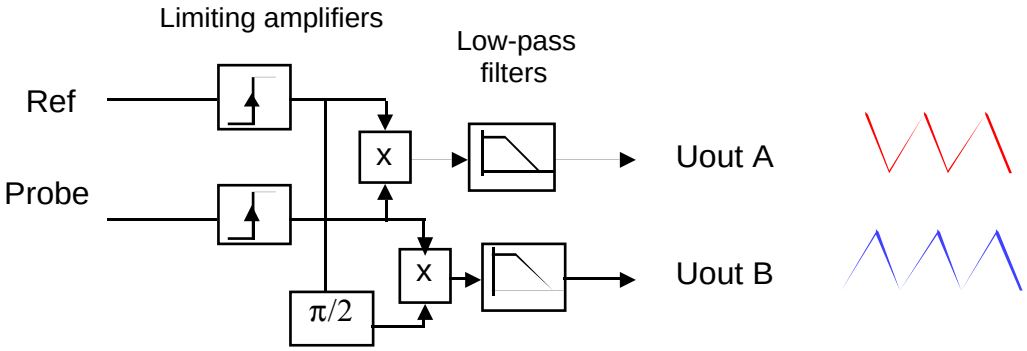

Figure 4.9 : Schematic layout of an analog phase demodulator.

4.4.3 Lock-in amplifier

Lock-in amplifiers are commonly used to extract small signals from noise. The technique of a lock-in amplifier is similar the analog phase demodulator, except for the limiting amplifiers. The reference and probe signals are directly mixed and low-pass filtered. As a result, we obtain two analog signals in quadrature, which depends on the amplitude r and phase ϕ of the probe signal, namely

$$X = r\cos\phi \quad \text{and} \quad Y = r\sin\phi. \tag{20}$$

The phase has therefore to be computed using the relation

$$\phi = \arctan\left(X/Y\right). \tag{21}$$

Therefore, the phase has to be computed from the two analog outputs X and Y by means of an A/D converter followed by a micro-controller board which calculates arctan(X/Y). On the other hand, the outputs of the analog phase demodulator described above are directly proportional to the phase. The phase measurement is therefore more direct for an analog phase demodulator than for a lock-in amplifier. Moreover, the analog phase demodulator works for a large range of signal levels (typically 5 mV to 5 V), whereas the pre-amplifier gain of the lock-in amplifier has to be adjusted to the signal level. Therefore, the analog phase demodulator seems to be more appropriate for phase measurement than a lock-in amplifier. However, the main drawback with

these two types of phase-meter is the need of a calibration. In addition, depending on the electrical components, electrical crosstalk and non-linearities may affect the phase measurement.

4.4.4 Digital zero-crossing phase-meter

The principle of a digital zero-crossing phase-meter is illustrated in Fig. 4.10. It consists of measuring the time interval between the leading edge of the reference signal and the one of the probe signal. For that purpose, a timebase signal of frequency f_c is used. A counter will measure the number of timebase cycles within this time interval. The reference starts the counter and the probe signal stops it. The value of this counter is then read-out immediately after a transition of the probe signal has occurred, simultaneously with the integer fringe counter. For ideal signals, the phase resolution is therefore limited by the timebase period. In the worst case, the phase error caused by the timebase frequency is

$$\delta\phi = 2\pi \frac{f}{f_c}. \tag{22}$$

The integer and fractional fringe counter values can be fed to accumulators, in order to compute an averaged value over a user-defined time interval T. This allows to perform $N = T f$ independent measurements. In that case, the errors caused by the timebase signal and by a limited SNR are reduced by a factor $\sqrt{T f}$, i.e.

$$\delta\phi_{av} = \sqrt{4\pi^2 \frac{f}{T f_c^{\,2}} + \frac{1}{T f SNR}}. \tag{23}$$

Such an averaging phasemeter has been developed by the Jet Propulsion Laboratory for Space Interferometry Mission [9].

The accuracy of the phase measurement depends also on the relative stability between the timebase frequency f_c and the superheterodyne frequency f. To avoid any drifts between f and f_c, the two signals must be synchronized. Synchronized signals are obtained by using phase-locked loops (PLL), or by using the timebase signal and frequency dividers for the generation of the heterodyne frequencies. In both cases, we obtain a timebase frequency $f_c = N_1 f$, where N_1 is an integer. Using Eq. (22), the phase resolution for ideal signals becomes then

$$\delta\phi = \frac{2\pi}{N_1}. \tag{24}$$

In order to get a phase resolution of $2\pi/1000$, the timebase frequency should be of at least 200 MHz for a heterodyne frequency of 200 kHz. Because of the synchronization, there is a

phase relation between the heterodyne and the timebase signals. As a result, the phase error given by Eq. (24) cannot be reduced by averaging over N periods. However, the phase error caused by the SNR can still be improved by averaging.

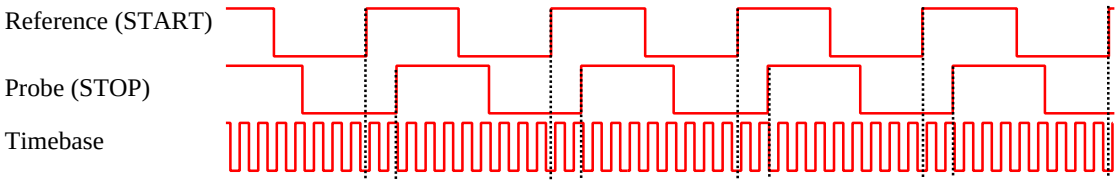

Figure 4.10: Timing diagram of a digital zero-crossing phasemeter

As already mentioned, the synchronization between the two signals can be obtained by dividing the timebase frequency to generate the heterodyne frequencies. In that case, the timebase frequency should be a multiple of the AOM frequencies. However, a timebase signal of 200 MHz cannot generate heterodyne frequencies of a few 100 kHz. Indeed, since the AOM frequencies are usually larger than 20 MHz, the minimal heterodyne frequency is obtained with frequency dividers of ratios 9 and 10 which generate AOM frequencies of 20 MHz and 22.2 MHz, respectively. We see that the corresponding minimal heterodyne frequency is higher than 2 MHz. A timebase frequency of at least 1 GHz is therefore required to generate the desired heterodyne frequencies. For instance, a timebase frequency of 1.1 GHz can be used to generate frequencies of 22 MHz, 22.45 MHz, 26.19 MHz and 26.83 MHz, with frequency dividers of 50, 49, 42 and 41, respectively. One gets then heterodyne frequencies f_1 of about 450 kHz and f_2 of about 640 kHz, and a superheterodyne frequency f = 190 kHz.

It may be more convenient to work with lower frequencies, and to choose the AOM frequencies with greater flexibility. In that case, the timebase signal of 200 MHz has to be generated from the reference signal of 200 kHz by means of phase-locked loop (PLL).

4.4.5 Digital phase-meter with Vernier technique

An alternative consists of a phase-locked loop to generate a timebase signal frequency f_c so that an integer number N_1 of heterodyne periods is equal to an integer number of timebase periods N_2 [6], i.e.

$$\frac{N_1}{f} = \frac{N_2}{f_c}. \qquad (25)$$

Phase measurement over a single period of the heterodyne signal will provide a phase resolution of $2\pi/N_1$, as expected from Eq. (24). However, by integrating over the interval $T = N_1/f$, we measure the phase with an error

$$\delta\phi = \frac{2\pi}{N_2} \tag{26}$$

in the worst case. Assuming $N_1 = 101$, $N_2 = 4096$, $f = 200$ kHz, we see that a clock frequency of only $f_c = 8.11$ MHz is required to achieve phase resolution of $2\pi/4096$ over an integration time $T = N_1/f = 0.5$ ms. Therefore, we see that a low-frequency timebase can be used with this Vernier technique to achieve resolution better than $2\pi/1000$. In addition, the phase error caused by the signal-to-noise ratio SNR is reduced by averaging over N_1 independent measurements. The phase accuracy over $T = N_1/f$ for a given SNR becomes therefore

$$\delta\phi_T = \sqrt{\frac{4\pi^2}{N_2{}^2} + \frac{1}{N_1 SNR}}. \tag{27}$$

4.4.6 Preferred concept

Analog phase demodulators and lock-in amplifiers have the advantage to be not limited by a timebase signal. However, the main drawback with analog techniques is the need of calibration and their sensitivity to thermal drifts. In addition, depending on the electrical components, electrical crosstalk and non-linearities may perturb the phase measurement.

Digital phase-meters are limited by the timebase period. A timebase frequency of 200 MHz is required to achieve $2\pi/1000$ resolution. However, this relatively high frequencies are supported by high-speed programmable logics (e.g. Altera, Actel). By synchronizing the timebase signal to the reference signal, no calibration is required. To avoid GHz frequencies, a phase-locked loop has been preferred to a single clock signal with frequency dividers. The preferred concept is shown in Fig. 4.11. Annex A shows a timing diagram for a constant velocity of the differential delay lines.

The summed integer and fractional numbers I and F will be divided by the number of measurements which have been read during the summation interval. Therefore, an additional counter should be used to count the number of transition of the signal “Read” during the summation interval.

Some problems may occur when the transition of the reference signal happens just after the transition of the probe signal: A new measurement may start before the last measurement is read-out. To solve this problem, the output of the counters must be read only within the time

interval between a probe transition and a reference transition. If a reference transition has just happened, the system must wait for the next probe transition [9].

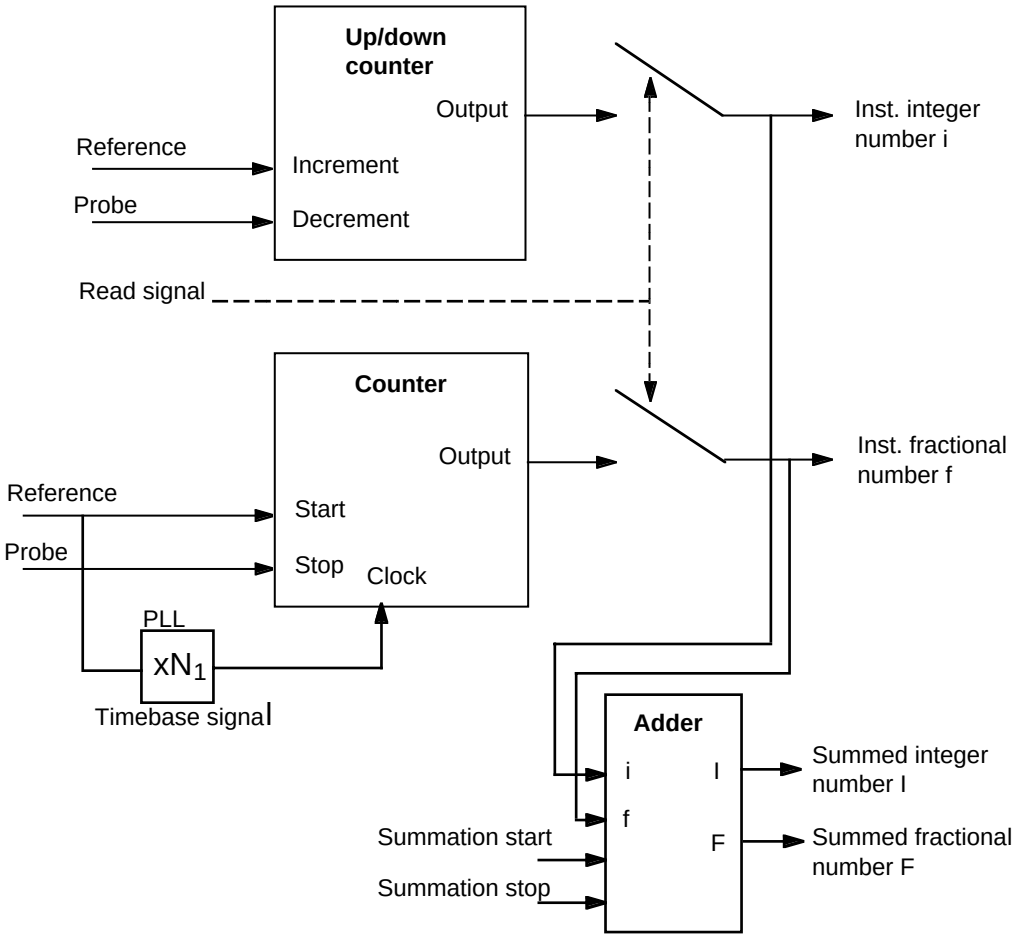

Figure 4.11: Schematic layout of the preferred concept for a digital phasemeter.

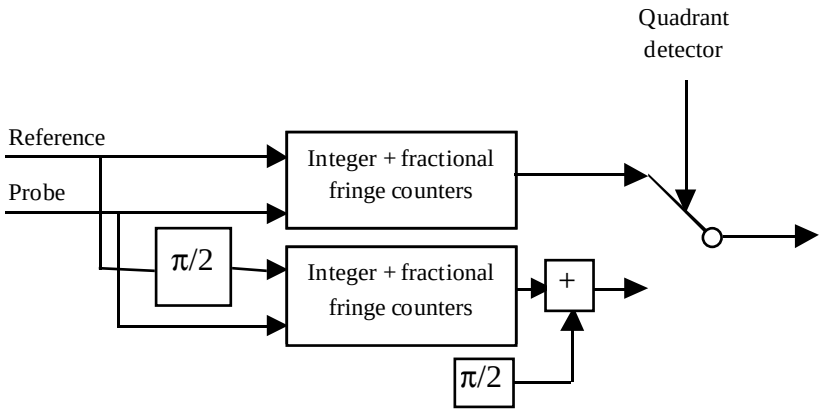

Figure 4.12: Schematic layout of the two output phasemeter.

Another solution consists of generating values which are phase shifted by 90°, by delaying the reference signal, as shown in Fig. 4.12. The 90° phase shift can be generated by doubling the frequency of the reference signal and feeding the doubled signal to an electronic Flip-Flop. This solution has been preferred since a measurement is always provided after each probe transition.

4.5 Commercial availability

Universal counters (e.g. Hewlett-Packard HP53131, Stanford Research 620) can be operated as phasemeters. However, an integer fringe counter has to be added to be able to measure the displacement over 120 mm. In addition, the measurement consists actually of two measurements, i.e. measurement of the time interval between the reference and probe transitions and measurement of the frequency of the reference signal. Instantaneous phase measurements are therefore difficult to obtain.

Zygo interferometers [10] use heterodyne detection. However, the system is designed to monitor high target speeds (up to 5 m/s). The heterodyne frequency is therefore very high (about 20 MHz) and a large detection bandwidth is used, which may limit the signal-to-noise ratio.

A custom designed phasemeter seems therefore to be the most promising approach for this type of application. General purpose timing boards (e.g. National Instruments Timing Boards) contain several counters which can be configured by software (e.g. Labview) for a specific application. Another solution consists of using programmable logics (e.g. Altera components) to realize the phasemeter. An additional phase-locked loop should be manufactured to synchronize the timebase signal to the heterodyne frequency.

4.6 Conclusions

A superheterodyne detection scheme has been selected to access directly to the differential optical path difference from the two individual interference signals. We showed that an appropriate choice of the heterodyne frequencies allows to suppress at the most possible crosstalks between the two interferometers. Heterodyne frequencies of 450 kHz and 650 kHz have been chosen, corresponding to a superheterodyne frequency of 200 kHz (see chapter 4.2.3).

We investigated the minimal optical power which is required to achieve the desired accuracy. We showed that for a fringe visibility of 80%, an optical power of 200 nW is high enough to achieve phase resolution better than $2\pi/600$.

The concept of a custom designed digital phasemeter has been established. The phasemeter allows to measure the phase instantaneously or to measure a mean value, obtained by averaging over an arbitrary number of cycles of the heterodyne signal. The phasemeter wouldn't require any calibration and wouldn't be sensitive to temperature. This is of a great interest in order to obtain a good day-to-day reproducibility. The overall diagram of the phase detection unit is shown in Annex B.

References

[1] Specifications for the feasibility study of the phase referenced imaging and micro-arcsecond astrometry facility (PRIMA), VLT-SPE-ESO-15800-1652

[2] ESO-VLTI Phase Referenced Imaging and Microarcsecond Astrometry facility, Feasibility Study, VLT-TRE-DSS-15700-0001

[3] PRIMA/FSU feasibility study, final report, VLT-TRE-ONE-15700-0001.

[4] Specifications for the PRIMA Metrology, Rider Study, VLT-SPE-ESO-15700-1959

[5] R. Dändliker, R. Thalmann and D. Prongué, " Two-wavelength laser interferometry using superheterodyne detection", *Opt. Lett.* **13**, 339-341 (1988).

[6] C Giunti, G. Margheri and S. Zatti in *Optical Surface Profile Monitor*, Final Report ESTEC no 8742/90/NL/PB(SC), pp. B2-41–B2-44.

[7] E. Zimmermann in *Signal Processing For Optical Phase Detection* (PhD Thesis, University of Neuchâtel, 1997), chap. 3.

[8] A. Yariv, *Optical Electronics 3rd ed.* (Holt-Saunders, New-York, 1985), pp. 306-320.

[9] P. G. Halverson, D. R. Johnson, A. Kuhnert, S. B. Shaklan and R. Spero, "A multi-channel averaging phasemeter for picometer precision laser metrology", *Proc. SPIE* **3740**, *conf. on Optical Engineering for Sensing and Nanotechnology (ICOSN'99), p. 646.*

[10] F. C. Demarest, "High-resolution, high-speed, low data age uncertainty, heterodyne displacement measuring interferometer electronics", *Meas. Sci. Technol.* **9**, 1024–1030 (1998).

5. Dispersion control

5.1. Refraction index of air : The Edlén Equation

The refraction index n of air is usually calculated by the updated Edlén equation[1]. For a proportion of 450 ppm of CO_2 in air, a temperature T in degree Celcius, and a pressure P in Pascal, it is

$$(n-1)_{TP} = \frac{P\,(n-1)_S}{96095.43}\,\frac{1+10^{-8}(0.601-0.00972\,T)\,P}{1+0.003661\,T}, \qquad (1)$$

where the refraction index $(n-1)_S$ for a wavelength λ, in dry air and standard conditions P = 101325 Pa and T = 15 °C, is

$$(n-1)_S \cdot 10^8 = 8343.05 + \frac{2406294}{130-\frac{1}{\lambda^2}} + \frac{15999}{38.9-\frac{1}{\lambda^2}}. \qquad (2)$$

The refraction index of moist air containing a partial pressure f in Pascal of water vapor is

$$n_{TPf} = n_{TP} - f\left(3.7345 - 0.0401\,\frac{1}{\lambda^2}\right)\cdot 10^{-10}, \qquad (3)$$

where f is derived from the relative humidity RH in percent by [2]

$$f = \frac{RH}{100}\left(4.07859739 + 0.44301857\,T + 0.00232093\,T^2 + 0.00045785\,T^3\right) \qquad (4)$$

Equations (1-4) were established for wavelengths between 350 nm and 650 nm, but they have been verified experimentally for a wider range of wavelengths. Table 1 is a summary of the experimental verifications of the Eldén equation reported in the literature. The uncertainty shows the agreement between the measured and the calculated value of the index of refraction, including the errors on the determination of the environmental parameters.

Wavelength (μm)	Uncertainty	Source
0.230 to 2.06	$\sigma \sim 10^{-8}$	Edlén 1965 [3]
0.350 to 0.650	$3\,\sigma = 3\cdot 10^{-8}$	Birch 1993 [1]
0.780	$< 2\cdot 10^{-7}$ (environmental parameters)	Khélifa 1998 [4]
3.39	$< 10^{-7}$	Matsumoto 1980 [5]
10.6	$\sigma \sim 10^{-8}$ for dry air not valid for moist air	Matsumoto 1984 [6]

Table 1. experimental verifications of the Eldén equation.

It arises that the Edlén Equation can be applied in dry air for the wavelengths ranging from 0.230 μm to 10 μm with an uncertainty in the order of 10^{-8}.

Within the range of environmental parameters representative of the external conditions over one night at Paranal (Table 2), the maximum relative variation of the index of refraction of air, calculated from equations (1-4), is

$$\frac{\Delta n}{n} \leq \begin{matrix} -7 \cdot 10^{-7} \ / \ °C \\ 2.7 \cdot 10^{-9} \ / \ Pa \\ -6.5 \cdot 10^{-9} \ / \ \%RH \end{matrix}, \tag{5}$$

Parameter	Minimum	Normal	Maximum
T (°C)	15	15.5	17.5
P (Pa)	74200	74300	74500
RH (%)	2	5	12

Table 2. Annual variation range of temperature T (°C), pressure P (Pa) and relative humidity RH (%) into the tunnels of the VLTI. These parameter are drawn from [7] and the ESO website.

The wavelength dependence of the index of refraction of air in normal conditions at Paranal (Table 2) is shown in Figure 1.

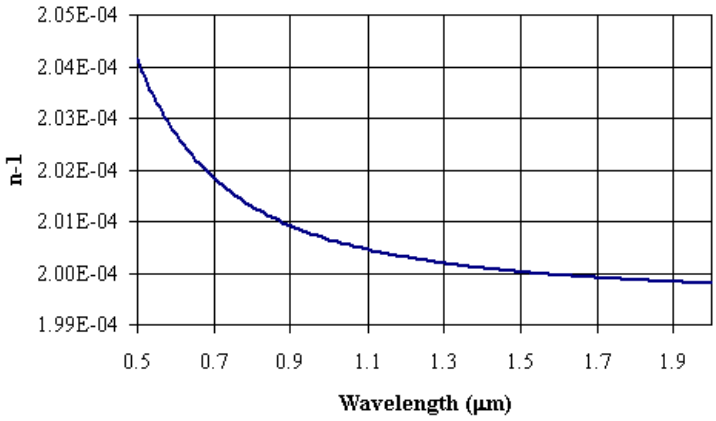

Figure 1. Refractive index of air vs. the wavelength, for T = 15.5 °C, P = 74300 Pa and RH = 5 %.

5.2. Measurement at a single wavelength

If we want to measure a geometrical path difference $D \leq 63$ mm with an accuracy $\Delta D = 5$ nm and consider in a first approach constant environmental conditions over the whole system, D is related to the measured optical path difference L by

$$D = \frac{L}{n}. \tag{6}$$

The maximum relative uncertainty allowed in that case for the refractive index of air is

$$\frac{\Delta n}{n} = \frac{\Delta D}{D} \leq 7.9 \cdot 10^{-8}, \tag{7}$$

which corresponds to an uncertainty on the environmental parameters (Eq.(5)) of

$$\Delta T = 0.11\,°C, \quad \Delta P = 29\ Pa, \quad \Delta HR = 12\,\%\,. \tag{8}$$

It is not possible to control the longitudinal variations of the environmental parameters along the optical paths of the telescopes with sufficient accuracy. But we can minimize the difference of length and environmental conditions between the two arms of one telescope. Then, the longitudinal variations along these beams influence the two interferometers in the same way and compensate.
Once we have determined the zero-OPD position by calibration, the path difference to be measured is only caused by the displacement L_{DDL} of the differential delay line, and depends only on the conditions in this delay line. The measured optical path difference is

$$L = L_{dp} + L_{DDL}\,. \tag{9}$$

With the measurement path D_{Mi} and the reference path D_{Ri} of the telescope i, the residual dead path, which is the origin of the incremental metrology, is

$$L_{dp} = \left(\int_{D_{M2}} n\,dl - \int_{D_{M1}} n\,dl \right) - \left(\int_{D_{R2}} n\,dl - \int_{D_{R1}} n\,dl \right). \tag{10}$$

If the differential delay line is placed in vacuum, we measure directly the geometrical OPD $D_{DDL} = L_{DDL}$.

The term L_{dp} must not vary during the measurements of more than the required accuracy of 5 nm. If the conditions vary in a different way along a given part ΔD of the two beams of one telescope, it will result in a variation of the optical distance L_{dp}

$$\Delta L_{dp} = (n_M - n_R)\Delta D \tag{11}$$

where n_M and n_R are the mean indexes along this part ΔD of the measurement and the reference beam, respectively. So, for one meter of beam, the index must not vary of more than $5 \cdot 10^{-9}$, which correspond to a variation of the environmental conditions of

$$\Delta T = 0.0071\,°C, \quad \Delta P = 1.85\ Pa, \quad \Delta HR = 0.77\,\% \tag{12}$$

at a wavelength of 1.064 μm. So it is crucial to have the same conditions of propagation on the reference and the measurement beam of each telescope.

5.3. Relation between optical lengths at different wavelengths

For a geometrical distance D, the optical length at the wavelength λ_1 is $L_1 = n_1 D$, where n_1 is the refraction index of air at λ_1. At a wavelength λ_2, the optical length corresponding to D is $L_2 = n_2 D$. So we have

$$L_2 = \frac{n_2}{n_1} L_1 = R_{12} L_1 \tag{13}$$

The ratio R_{12} has the advantage to be more than two orders of magnitude less sensitive to the environmental conditions than the refraction index itself. In the range of environmental conditions of Table 2, for $\lambda_1 = 1.064$ μm and $\lambda_2 = 2.0$ μm, we get

$$\frac{\Delta R_{12}}{R_{12}} \leq \begin{matrix} 2.5 \cdot 10^{-9} \ / \ °C \\ -9.6 \cdot 10^{-12} \ / \ Pa \\ -4.47 \cdot 10^{-11} \ / \ \%HR \end{matrix} . \tag{14}$$

So it is possible to convert an optical length measured at one wavelength ($\lambda_1 = 1.064$ μm) to an optical length at another wavelength ($\lambda_2 = 2.0$ μm) with relaxed requirements on the knowledge of the environmental conditions along this path.

In our case, the light from a star falls on the two telescopes with an external path difference in vacuum D_{Vac}. This OPD is compensated by introducing an internal path difference $n_{Star} D_{DL}$ with the main delay lines, where n_{Star} is the refraction index of air at the working wavelength of the FSU and D_{DL} is the geometrical OPD introduced by the delay lines. D_{DL} is measured simultaneously by the metrology at 1.064 μm, which gives an optical distance $L_{Met} = n_{Met} D_{DL}$. So we have

$$D_{Vac} = n_{Star} \ D_{DL} = \frac{n_{Star}}{n_{Met}} L_{Met} . \tag{15}$$

As the stellar light and the metrology beams travel along the same paths at the same time, we can measure the OPD at the stellar wavelength with little sensitivity to the environmental conditions, according to Eq. (14).

5.4. Two-wavelength interferometry

5.4.1. Measurement of the geometrical path difference

We have seen in §5.2. that the determination of the geometrical path difference between the two arms of one interferometer from the optical length measured at one wavelength requires an extremely severe control of the environmental parameters. In the method described here, this geometrical path difference is obtained from independent measurements made simultaneously at two different wavelengths. It has the advantage of a low sensitivity to the environmental parameters.

If λ_1 and $\lambda_2 < \lambda_1$ are the wavelengths of the beams injected in the interferometer, for a geometrical path difference D, we measure the phases

$$\begin{aligned} \phi_1 &= 2 \frac{2\pi}{\lambda_1} L_1 \\ \phi_2 &= 2 \frac{2\pi}{\lambda_2} L_2 \end{aligned} . \tag{16}$$

where the optical path differences at λ_1 and λ_2 are, respectively,

$$\begin{aligned} L_1 &= n_1 \, D \\ L_2 &= n_2 \, D \end{aligned}. \tag{17}$$

Using a first-order approximation of the Eldén Equation for the refraction index of air, the geometrical distance D can be calculated by [8]

$$\begin{aligned} D &= L_2 - A(L_2 - L_1) \\ &= \frac{1}{4\pi}\left[A \, \lambda_1 \, \phi_1 + \lambda_2 \, \phi_2 \, (1 - A)\right]. \end{aligned} \tag{18}$$

where

$$A = \frac{n_2 - 1}{n_2 - n_1}. \tag{19}$$

This parameter A is not very sensitive to the environmental parameters. For $\lambda_1 = 1.064$ μm, $\lambda_2 = 0.532$ μm and $D = 63$ mm, the maximum error on the measured geometrical distance D due to the variations of the environmental parameters, in the range of the conditions in Table 2, is

$$\frac{\Delta D}{D} \leq \begin{matrix} -2.5 \cdot 10^{-7} / nm \, (\lambda_2) \\ -7 \cdot 10^{-9} / °C \\ 1.2 \cdot 10^{-12} / Pa \\ -1.9 \cdot 10^{-8} / \%HR \end{matrix}. \tag{20}$$

The error on the measured distance ΔD due to the phase measurement uncertainty

$$\Delta\phi_1 = \frac{2\pi}{N_1} \tag{21}$$

is

$$\Delta D = \frac{1}{4\pi} A \, \lambda_1 \, \Delta\phi_1 = \frac{1}{2} A \, \lambda_1 \, \frac{1}{N_1}. \tag{22}$$

The term $N_1 \Delta D$ is plotted in Figure 2 in function of λ_2, for $\lambda_1 = 0.632$ μm, $\lambda_1 = 1.064$ μm and $\lambda_1 = 2.0$ μm, respectively. For a phase measurement accuracy $\Delta\phi_1 = 2\pi/1000$ ($N_1 = 1000$), $\lambda_1 = 1.064$ μm and $\lambda_2 = 532$ nm, we get $\Delta D = 35$ nm. Under these conditions, $\Delta D = 5$ nm would be reached for $\lambda_2 < 210$ nm.

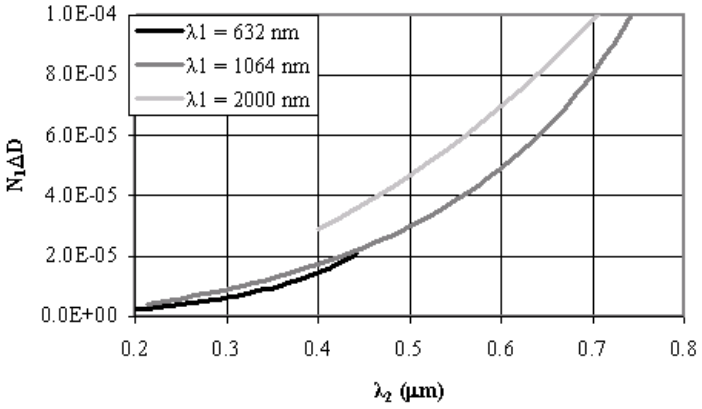

Figure 2. Error term $N_1\Delta D$ vs. λ_2 for $\lambda_1 = 0.632$ μm, $\lambda_1 = 1.064$ μm and $\lambda_1 = 2.0$ μm.

In conclusion, it is difficult to reach the required accuracy with this method, and it is possible only if visible or ultraviolet wavelengths can be used.

5.4.2. Measurement of the optical path difference

The two-wavelength technique can be also applied to determine the optical path difference at the stellar wavelength, L_S. Starting from Eq. (18), one can write

$$L_S = L_1 + \frac{A_{12}}{A_{1S}}(L_2 - L_1), \tag{23}$$

where $A_{12} = (n_2 - 1)/(n_2 - n_1)$ and $A_{1S} = (n_S - 1)/(n_S - n_1)$ respectively. The factor A_{12}/A_{1S} is much closer to unity that the factor A of Eq. (18), so it does not amplify the phase error in the same way (Eq. (22)). But this method appears to be more sensitive to the environmental parameters that the ratio of the indexes of refraction (Eq. (13)). For example, with $\lambda_S = 2$ μm, $\lambda_1 = \lambda_{Metrol} = 1.064$μm, $\lambda_2 = 0.532$ μm, $T = 15.5$°C, $P = 74300$ Pa, $RH = 5\%$, $D = 63$ mm, the relative error on the measurement of L_s with Eq. (23) is $-4.9\cdot10^{-9}$ / °C. If you use Eq. (13), this relative error reduces to $-2.4\cdot10^{-9}$ / °C. The reason is that in the first case, you make an error in the determination of 3 indexes of refraction, against 2 in the second case.

5.5. Second-Harmonic Interferometry

The purpose of this method [9] is to measure the mean refraction index along an optical path of known (or constant) length. The principle is shown on Figure 3.

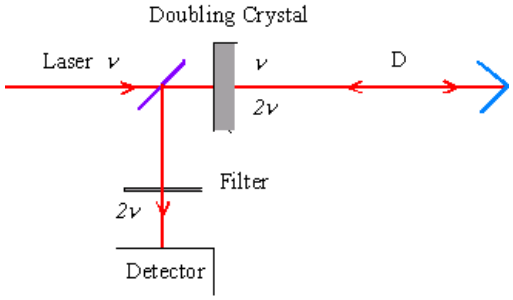

Figure 3. Principle of second harmonic interferometry.

The beam of the laser at frequency ν is partially doubled in frequency by a non-linear crystal. frequencies ν and 2ν propagate forth and back along the measurement path and are once again partially doubled in frequency, so we get one component at frequency ν, two at frequency 2ν and one at frequency 4ν. A filter selects the two components at frequency 2ν whose phase are, respectively,

$$\phi_{2\upsilon} = \frac{2\pi}{\lambda/2} 2\int_D n_{\lambda/2} dl \tag{24}$$

for the beam which has traveled along the path at frequency 2ν, and

$$2\,\phi_{\upsilon} = 2\left(\frac{2\pi}{\lambda} 2\int_D n_{\lambda} dl\right) \tag{25}$$

for the beam which has traveled along the path at frequency ν and has been then doubled in frequency. Their interference on the detector results in a phase difference

$$\begin{aligned}\phi &= \phi_{2\upsilon} - 2\,\phi_{\upsilon} \\ &= 4\frac{2\pi}{\lambda}\int_D \left(n_{\lambda/2} - n_{\lambda}\right) dl\,.\end{aligned} \tag{26}$$

If we neglect the dependence on the wavelength λ in Eq. (3), the Edlén Equation for the refraction index of air (Eqs. (1-4)) is of the form

$$n(\lambda, T, P, HR) = 1 + [n(\lambda) - 1]F(T, P) - G(RH) \tag{27}$$

where $n(\lambda)$ is the refraction index for standard conditions, $F(T, P)$ is a function of the temperature T and the pressure P, and $G(RH)$ is a function of the relative humidity RH. Using Eq. (27), the phase ϕ of Eq. (26) becomes

$$\phi = \phi_{2\upsilon} - 2\,\phi_{\upsilon} = 4\frac{2\pi}{\lambda}[n(\lambda/2) - n(\lambda)]\int_D F(T, P)\, dl \,. \tag{28}$$

Introducing

$$\langle F(T, P)\rangle = \frac{1}{D}\int_D F(T, P)\, dl \tag{29}$$

and replacing it in Eq. (27) by the expression from Eq. (28), we get the mean value over the path D of the index of refraction at an arbitrary wavelength λ_1,

$$\langle n(\lambda_1, T, P, RH)\rangle = 1 + \frac{n(\lambda_1) - 1}{n(\lambda/2) - n(\lambda)}\frac{\lambda\,\phi}{8\,\pi\,D} + G(RH)\,. \tag{30}$$

The error due to a phase measurement uncertainty of $\Delta\phi = 2\pi/N$ is

$$\Delta\langle n\rangle = \frac{n(\lambda_1)-1}{n(\lambda/2)-n(\lambda)}\frac{\lambda}{4\,D\,N}, \tag{31}$$

which has the same form as Eq. (22) with $\lambda_1 = \lambda/2$. For $\lambda_1 = \lambda = 1.064$ μm, $D = 100$ m and $\Delta\phi = 2\pi/1000$, Eq. (31) gives

$$\Delta\langle n\rangle \approx 1.8\cdot 10^{-10}, \tag{32}$$

and for $\lambda_1 = \lambda = 2.0$ μm,

$$\Delta\langle n\rangle \approx 1.9\cdot 10^{-9}. \tag{33}$$

This method gives good results for the determination of the mean refraction index over a long path, but D must be known. More interesting here, it can be also used to monitor the temporal variations of the environmental conditions along a given-length path.

In the context of the VLTI, we cannot generate the harmonics of the returning beams with a non-linear crystal (Figure 3) because there is not enough power to have a good conversion efficiency at the interferometer output. But we found that the same result can be reached with a superheterodyne technique [10]. In that case, the doubling crystal is placed in front of the laser source to generate the two wavelengths λ and λ/2. Then, a frequency shifter module, composed of acousto-optics modulators, produces two different heterodyne frequencies f_1 and f_2 for λ and λ/2, respectively. The interference signal at the output of the detector is a sum of two components,

$$\begin{aligned} I_1 &= \cos(2\pi f_1 t + \phi_v) \\ I_2 &= \cos(2\pi f_2 t + \phi_{2v}), \end{aligned} \tag{34}$$

which can be separated electronically. By doubling electronically the frequency f_1 and phase ϕ_v of the signal I_1, mixing the two signals and bandpass filtering around $(2f_1 - f_2)$, we obtain

$$I_{12} = \cos\left[2\pi(2f_1 - f_2)t + 2\phi_v - \phi_{2v}\right]. \tag{35}$$

The phase difference $\phi = 2\phi_v - \phi_{2v}$, which is the same as Eq. (28), can then be measured with a phasemeter.

5.6. Conclusion

The Edlèn Equation (§5.1) can be used to calculate the index of refraction of air at all wavelengths from 0.230 μm to 10 μm, with an accuracy in the order of 10^{-8}.

To measure the geometrical path difference, the best solution is to use a evacuated differential delay line, and to make frequent calibrations of the zero of the metrology (§5.2). However, the

requirements on the stability of the environmental parameters along the paths are extremely severe and will be very difficult to reach. The determination of this geometrical path difference from independent measurements at two wavelengths with the method described in §5.4 is not accurate enough here.

The optical path difference at the stellar wavelength is easier to measure. The best way to determine it from the OPD measured at the wavelength of the metrology it to use the ratio of the indexes of refraction at the two wavelengths, as described in §5.3. The sensitivity of this index ratio to the environmental parameters is two orders of magnitude smaller than the indexes themselves, as long at the metrology and stellar beams share the same paths. It remains that, because of the length of the paths (§5.2), the environmental control requirements are still high.

The best principle to monitor the temporal variations of the conditions of propagation along a path is the second harmonic interferometry. We cannot use here the classical set-up involving a non-linear crystal. So we propose an innovative approach, the Electronic Second Harmonic Interferometry, which is described in §5.5 and could lead to a patent.

So, in conclusion, our preferred solution to solve the problem of the dispersion is to

- Make the metrology beams travel along the same paths as the stellar light,
- Calculate the optical path difference at the stellar wavelength from the OPD measured at the wavelength of the metrology by using the ratio of the indexes of refraction,
- Monitor the temporal variations of the conditions of propagation along all arms of the interferometers with the Electronic Second Harmonic Interferometry method.

However, we must keep in mind that we are very close to the limit of validity of the Edlèn Equation, so further experimental verifications and a breadboard demonstrator will be required to determine the most efficient solution.

---

[1] K. P. Birch, M. J. Downs, "An Updated Edlén Equation for the Refractive Index of Air", *Metrologia* **30:**155-162 (1993)

[2] Zygo, *A Primer on Displacement Measuring Interferometers* (Zygo, Laurel Brook Road, Middlefield, Connecticut, 06455-0448, USA) p. 57.

[3] B. Edlén "The Refractive Index of Air" *Metrologia* **2** (2):71-80 (1966).

[4] N. Khélifa, H. Fang, J. Xu, P. Juncar, H. Himbert, "Refractometer for tracking changes in the refractive index of air near 780 nm" *Appl. Opt.* **37**(1):156-161 (1998).

[5] H. Matsumoto "Length measurement of Bauge Blocks Using a 3.39 μm He-Ne laser Interferometer" *Japan. J. Appl. Phys.* **19**(4):713-718 (1980).

[6] H. Matsumoto "The refractivities of water vapour for CO_2 Laser Lines" *Opt. Com.* **50**(6):356-358 (1984).

[7] S. Lévêque, B. Koehler, "Result of the environmental tests inside the interferometric tunnel Paranal 12-21/5/99" ESO Report, 1999.

[8] A. Ishida "Two-wavelength Displacement-Measuring Interferometer Using Second-Harmonic Light to Eliminate Air-Turbulence-induced Errors" *Japan. J. Appl. Phys.* **28**(3):L473-L475 (1989 March)

[9] N. Bretz, F. Jobes, J. Irby, "The design of a second harmonic tengential array interferometer for C-Mod" *Rev. Sci. Instrum.* **68**(1):713-716 (1997 January).

[10] R. Dändliker, R. Thalmann and D. Prongué, " Two-wavelength laser interferometry using superheterodyne detection", Opt. Lett. 13, 339-341 (1988).

6 White-light interferometry for internal calibration

6.1 Principle

The use of a commercially available low-coherent source should allow to calibrate the zero-internal OPD without the need of the star separator. The concept is depicted in Fig. 6.1. The light is first injected in the reference interferometer, and is then fed into the science interferometer by means of a fiber link. White-light fringes will be observed at the output when the OPD of the science interferometer is equal to the OPD of the reference interferometer. The availability of white-light source around 1.5 µm (Superluminescent diode, Erbium doped fiber) permits to use directly the secondary FSU for processing the white-light fringes. In this way, the light of the low-coherent source can be co-linear to the starlight.

6.2 Detection technique

The concept depicted in Fig. 6.1 is equivalent to two Michelson interferometers in tandem configuration, as shown in Fig. 6.2.

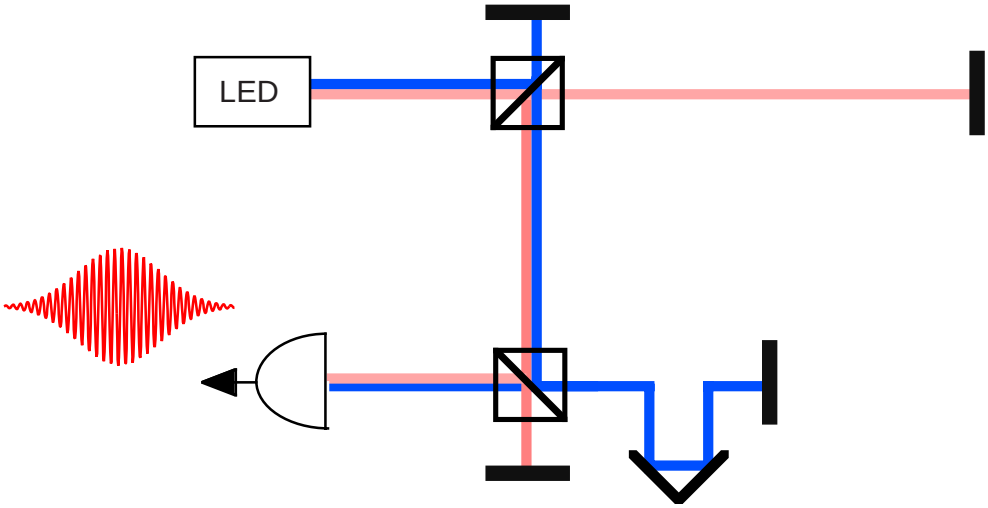

Figure 6.2: Michelson interferometers in tandem configuration. White light fringes can be observed with a visibility of max. 50% when the solid path length is equal to the dotted one.

Different solutions are possible for the detection technique. We propose here a scanning approach with FFT analysis, which has been successfully tested for position measurement [1]. The principle consists of scanning the differential delay line and recording the white-light

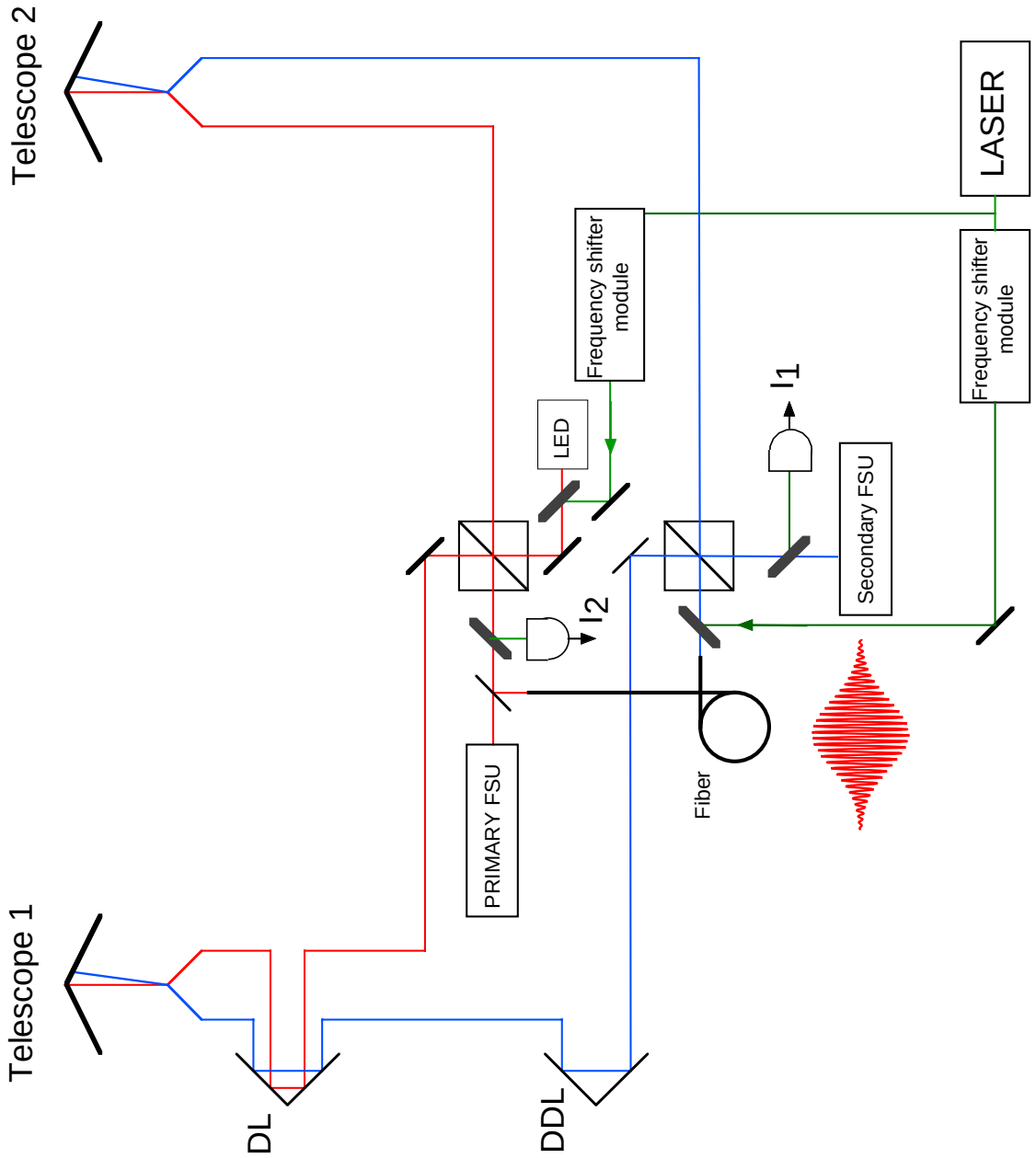

Figure 6.1: Set-up for internal calibration by white-light interferometry.

fringes as a function of the laser interferometer results. The laser metrology and the white-light interferometer must work simultaneously to overcome the effects of internal turbulence. The laser interferometer triggers the Fringe Sensor Unit. An accurate displacement scale is obtained in this way. A Fast Fourier Transform (FFT) of the recorded interference signal allows to obtain the power spectrum, and the phase $\phi(\nu)$ as a function of the optical frequency. The center of gravity L of the interference signal can then be deduced from the slope of $\phi(\nu)$. Indeed, we have

$$\phi(\nu) = \frac{2\pi}{c}\nu \ \ 2L \tag{1}$$

The distance is therefore given by

$$L = \phi'(\nu)\frac{c}{4\pi}, \tag{2}$$

where $\phi'(\nu) = d\phi/d\nu$.

Preliminary measurements were performed during previous studies. Typical interference signal is shown in Fig. 6.3 as a function of the optical path difference. The source was a LED emitting at 890 nm and with a spectral width of 50 nm. In this experiment, one of the mirror of the second interferometer was scanned by means of calibrated piezo-transducer. Figure 6.4 shows the result of the FFT, and especially the unwrapped phase $\phi(\nu)$ as a function of the optical frequency. Preliminary tests showed a repeatability of 20 nm, but was probably limited by the mechanical stability of the experimental set-up.

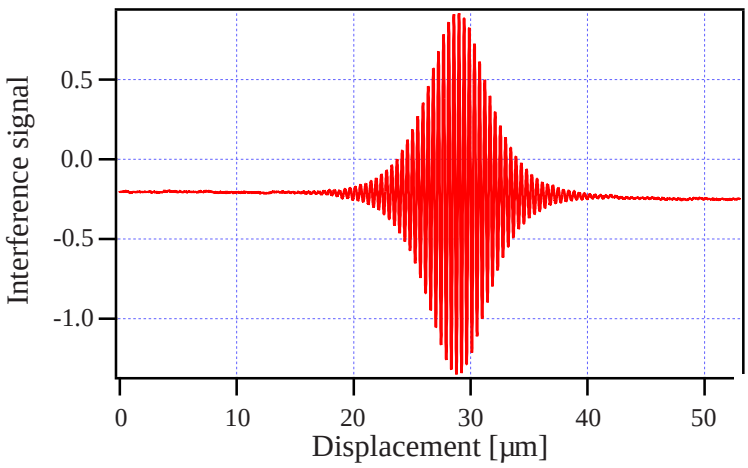

Figure 6.3: Typical interference signal

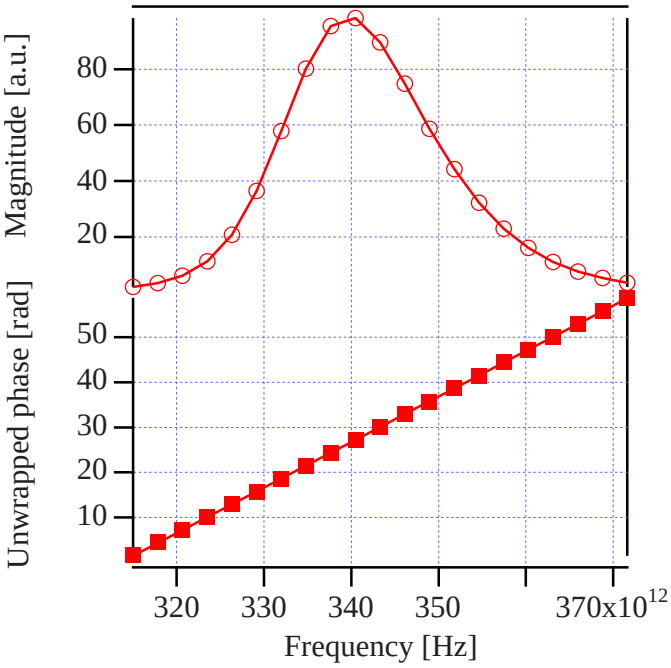

Figure 6.4: FFT of the interference signal

6.3 Calibration procedure

A new procedure can be considered for the calibration of the zero-OPD:

1) Pre-position the delay line, using the *a-priori* knowledge of the optical path difference required to observe stellar fringes on the primary FSU.

2) Start the laser interferometers at an arbitrary position of the differential delay line.

3) Switch on the internal white-light source.

4) Scan the differential delay line in order to determine roughly the position of the white-light fringes on the secondary FSU (caused by the internal white-light source).

5) Position the differential delay line close to these white-light fringes.

6) Scan slowly the differential delay line over a scan length of a few 50 μ, and record the interferogram.

7) Perform a Fast-Fourier Transform of the sampled interferogram, and determine the center of gravity of the signal. During this calculation, the laser metrology must not be interrupted to be able to monitor the possible OPD variations.

8) Subtract this value to the differential OPD measured by the laser metrology, to obtain a calibrated measurement of the differential optical path difference.

9) Switch off the internal white-light source, and tracked the stellar white-light fringes.

6.4 Fiber link

The two interferometers can be linked by means of an optical fiber. Since the beam has to propagate over large distances (> 400 m) a single spatial mode fiber is mandatory. In this way, the fiber will act as a spatial filter. However, the coupling efficiency may be low, depending on the wavefront distortions caused by the internal air turbulence. This problem is also encountered when coupling the light to the FSU, since the FSU involves single mode fibers [3]. The adaptive optics may help to correct the wavefronts and to optimize these coupling efficiencies.

Since the interferring beams share the same path in the fiber link, the stability of the fiber length is not required.

6.5 Simulations

The noise level on the amplitude of the FFT depends on the rms noise V_{rms} of the interference signal divided by the square root of the number of samples N, i.e.

$$\hat{V}_A^{noise}(\nu) = \frac{V_{rms}}{\sqrt{N}}. \tag{3}$$

Therefore, a large number of samples N allows to reduce the noise level in the FFT. On the other hand, the maximal value of the amplitude spectrum $\hat{V}(\nu)$ depends on the quadratic mean of the interference signal. This quadratic mean depends on the ratio between the scan length L_{scan} and the coherence length L_c of the source, assuming that $L_{scan} >> L_c$. Since the coherence length is inversely related to the spectral width $\Delta\lambda$, we have

$$\hat{V}(\nu) \propto \frac{V}{\Delta\lambda\, L_{scan}} \sqrt{S(\nu)}, \tag{4}$$

where V is the maximal amplitude (0 to peak) of the interference signal, and $S(\nu)$ is the normalized power spectrum of the source. A phase error will be introduced for each frequency in the Fast Fourier Transform, depending on the ratio between V_A^{noise} and $\hat{V}(\nu)$, namely

$$\delta\phi(\nu) \approx \frac{V_A^{noise}(\nu)}{\hat{V}(\nu)}. \tag{5}$$

These phase errors will then introduce a distance error δL on the zero-OPD calibration. The relation between the distance resolution and the phase resolution will depend on the spectral width and on the number of points within this spectral width. The accuracy depends therefore on

the following parameters: The signal-to-noise ratio at the maximal value of the interference signal $SNR_{max} = (V/V_{rms})^2$, the number of points of the recorded interferogram N, the scan length L_{scan}, and the spectral width $\Delta\lambda$ (full width at half maximum). Numerical simulations were performed using the software Labview. The program allows to generate a noisy interference signal which depends on user defined values of SNR_{max}, N, L_{scan}, $\Delta\lambda$ and the position L. The center of gravity is then detected by FFT analysis. From 100 independent simulations, we have evaluated the accuracy of the technique.

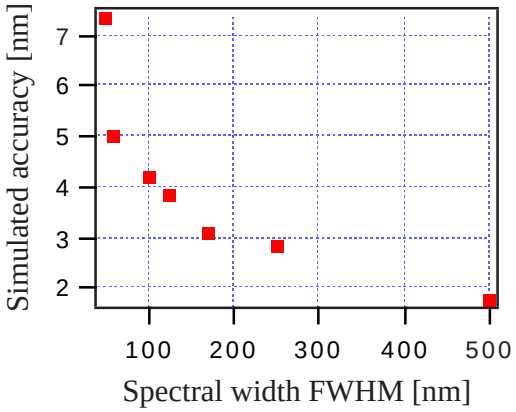

Figure 6.5: Simulated accuracy for different $\Delta\lambda$; L_{scan} = 50 µm, L = 25 µm, SNR_{max} = 40 dB, N = 4096.

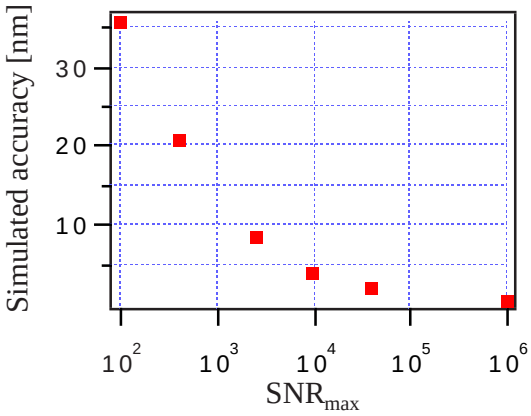

Figure 6.6: Simulated accuracy for different SNR_{max}; L_{scan} = 50 µm, L = 25 µm, $\Delta\lambda$ = 100 nm, N = 4096.

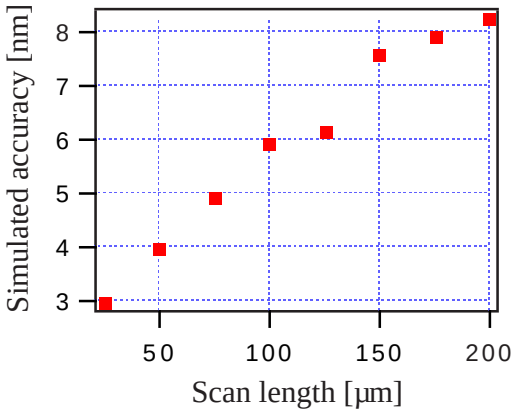

Figure 6.7: Simulated accuracy for different L_{scan}; L = 12 µm, SNR_{max} = 40 dB, $\Delta\lambda$ = 100 nm, N = 4096.

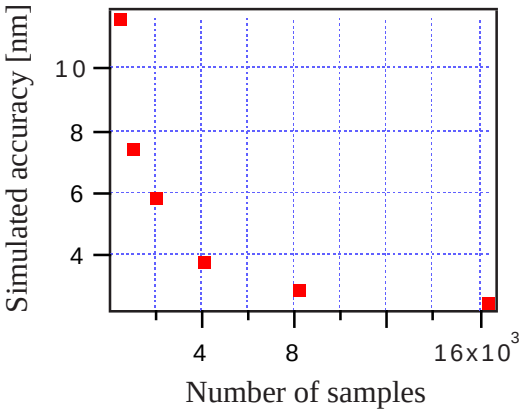

Figure 6.8: Simulated accuracy for different N; L_{scan} = 50 µm, L = 25 µm, SNR_{max} = 40 dB, $\Delta\lambda$ = 100 nm.

Figures 6.5–6.8 show the dependence of the parameters SNR, N, L_{scan}, and $\Delta\lambda$. The accuracy does not depend on the position of the interferogram, as long as the interference signal is not truncated by window effects. When pre-positioning the differential line (step 5 of the calibration procedure) care must be taken that

$$L_{coh} < L < L_{scan} - L_{coh}, \tag{6}$$

where L_{coh} is the coherence length of the source. For a Gaussian spectral lineshape, the coherence length is defined as [2]

$$L_{coh} = \frac{\lambda^2}{\Delta\lambda}\sqrt{2\ln 2/\pi}. \tag{7}$$

The spectral width and the SNR_{max} should be as large as possible to achieve a high accuracy, as shown in Figs. 6.5 and 6.6. A trade-off must be made for the scan length: as already mentioned, the scan length must be larger than the coherence length to avoid window effects, but we see from Fig. 6.7 that a too large scan length will affect the accuracy. From Fig. 6.8, we see also that a large number of samples helps to achieve a high accuracy, since the noise level of the FFT is reduced (Eq. (3)). The desired accuracy (5 nm) can be obtained with a scan length of about 50 µm, a SNR_{max} of 40 dB, a spectral width of 100 nm and a number of points of 4096. Therefore, the spacing between two consecutive samples should be of about 15 nm. Since the laser metrology is expected to have an accuracy better than 5 nm, such spacing should be feasible.

6.6 Power limitation

A signal-to-noise ratio of at least 40 dB is required to achieve the desired accuracy (see Fig. 6.6). A minimal power is therefore required on the FSU. Since the noise of the FSU is expected to be very small (less than 10 electrons) [3], the detection will be mainly limited by the shot noise. The variance of the shot noise is equal to the mean number of photo-electrons $\bar{n}$. On the other hand, the electrical power of the signal is proportional to the square of the fringe visibility m and to the square of the mean number of photo-electrons. The signal-to-noise ratio at the maximal value of the interference signal is therefore

$$SNR_{max} = m^2\bar{n}. \tag{8}$$

The number of photons n_p which arrive onto the detector during the observation time T is given by

$$\bar{n}_p = \frac{\bar{n}}{\eta}, \tag{9}$$

where η is the quantum efficiency of the detector. In order to get a SNR of 40 dB, we see from Eqs (8)–(9) that a number of photons

$$\bar{n}_p = \frac{10'000}{\eta\ m^2} \tag{10}$$

is required. The quantum efficiency η of the Fringe Sensor is expected to be about 50% around 1.5 µm [3]. The maximal visibility which can be obtained with the configuration described in Fig. 6.2 is of 50%. In this ideal case, we found $n_p = 80'000$, corresponding to 40'000 photo-electrons. The FSU will be composed of several pixels, which have an integration capacity of 100'000 electrons. For a maximal fringe visibility (50%), measurement on a single pixel should therefore be feasible.

For a fringe visibility of 20%, the required number of photo-electrons is $2.5 \cdot 10^5$, which is much higher than the integration capacity of one pixel. To solve this problem, the interference signal can be detected with several pixels, by defocusing the image on the detector. For instance, the integration capacity is increased to $4 \cdot 10^5$ by detecting with 4 pixels. However, it would be difficult to achieve the desired accuracy for contrasts lower than 20%. Care must be taken to achieve therefore the best fringe visibility. The adaptive optics could possibly be used to optimize the fringe visibility.

The integration time per sample of the interferogram should be short enough because of the internal air turbulence. An integration time of 1 ms per sample should be reasonable. In that case, the required optical power for $m = 0.5$ is

$$P_{opt,min} = 80'000 \frac{h\nu}{T} = 10 \text{ pW}. \tag{11}$$

The required input optical power of the internal white-light source depends on the losses through both interferometers. These losses may be caused by the diffraction, the coupling efficiency in the single mode fiber link, and the coupling to the FSU. Assuming a transmitivity of 0.01% though the whole set-up, an input power of a few 100 nW seems to be high enough to get a signal-to-noise ratio of 40 dB.

In order to avoid background light on the FSU, the laser beam of the metrology must be efficiently separated from the white-light. Since the laser beam will overlap the white-light beam, they must be spectrally separated by means of dichroic beamsplitters. Typical efficiency of such

components is of 99.5% in reflectance (e.g. CVI dichroic mirrors). Assuming an optical power for the metrology beam of a few µW, the remaining 0.5% optical power which is transmitted is still much higher than the integration capacity of the FSU. Several dichroic mirrors in cascade (at least 3) should be used to suppress at the most the laser metrology beam.

The possible intensity fluctuations during the measurement of the interference signal may also limit the measurement accuracy. The two outputs of the beam combiner, which are phase-shifted by π, should be used to solve this problem. Indeed, the two signals can be subtracted to suppress the DC offset and thus to minimize the effects of intensity fluctuations.

6.7 Source availability

As shown in Fig 6.5, the white-light source must exhibit a spectral width of at least 100 nm. Since the beam has to propagate over large distances (> 400 m) a single spatial mode light source is mandatory. Two types of source can be foreseen: The amplified spontaneous emission (ASE) of Erbium doped fiber at 1.5 µm (i) and Light-emitting or super-luminescent diode (LED) (ii). Fiber light sources can provide relatively high power (10 mW) but a flat spectrum may be difficult to obtain. In addition, the spectral width of commercially available fiber light source is limited to 73 nm to our knowledge (EXFO model IQ-2300). Surface emitting LED at 1.55 µm can provide a larger spectral width of 100–120 nm. However, only a few µW optical power can be launched into a single mode fiber. Edge-emitting (or superluminescent) LEDs provide a few 100 µW into single mode fibers, but exhibit spectral widths of 50–60 nm. An attractive solution consists of using two pigtailed superluminescent LEDs with slightly different center wavelengths. For instance, the incoherent superposition of two superluminescent LEDs emitting at 1.55 µm and 1.65 µm (e.g. NEL Superluminescent Diodes, models no NLK1690BTP and NLK1590BTD) can provide 150 nm spectral width.

6.8 Conclusion

A new calibration procedure of the zero-OPD is proposed, based on white-light interferometry. A detection technique based on FFT analysis should enable the desired accuracy, provided that the signal-to-noise ratio is at least 40 dB and that the spectral width is at least 100 nm. For the white-light source, we propose to use two commercially available pigtailed superluminescent diodes emitting at slightly different center wavelengths. Using the FSU as detector, a minimal optical power of 10 pW is required at the output.

Experimental tests of accuracy are recommended to verify the reliability of this technique.

References

[1] A. Koch and R. Ulrich, “Fiber-optic displacement sensor with 0.02 µm resolution by white-light interferometry”, Sensors and Actuators A 25-27, 201–207 (1991).

[2] J. W. Goodman in *Statistical Optics* (Wiley & Sons, New York, 1985), chap. 5.1.3

[3] PRIMA/FSU feasibility study, final report, VLT-TRE-ONE-15700-0001.

Annex A

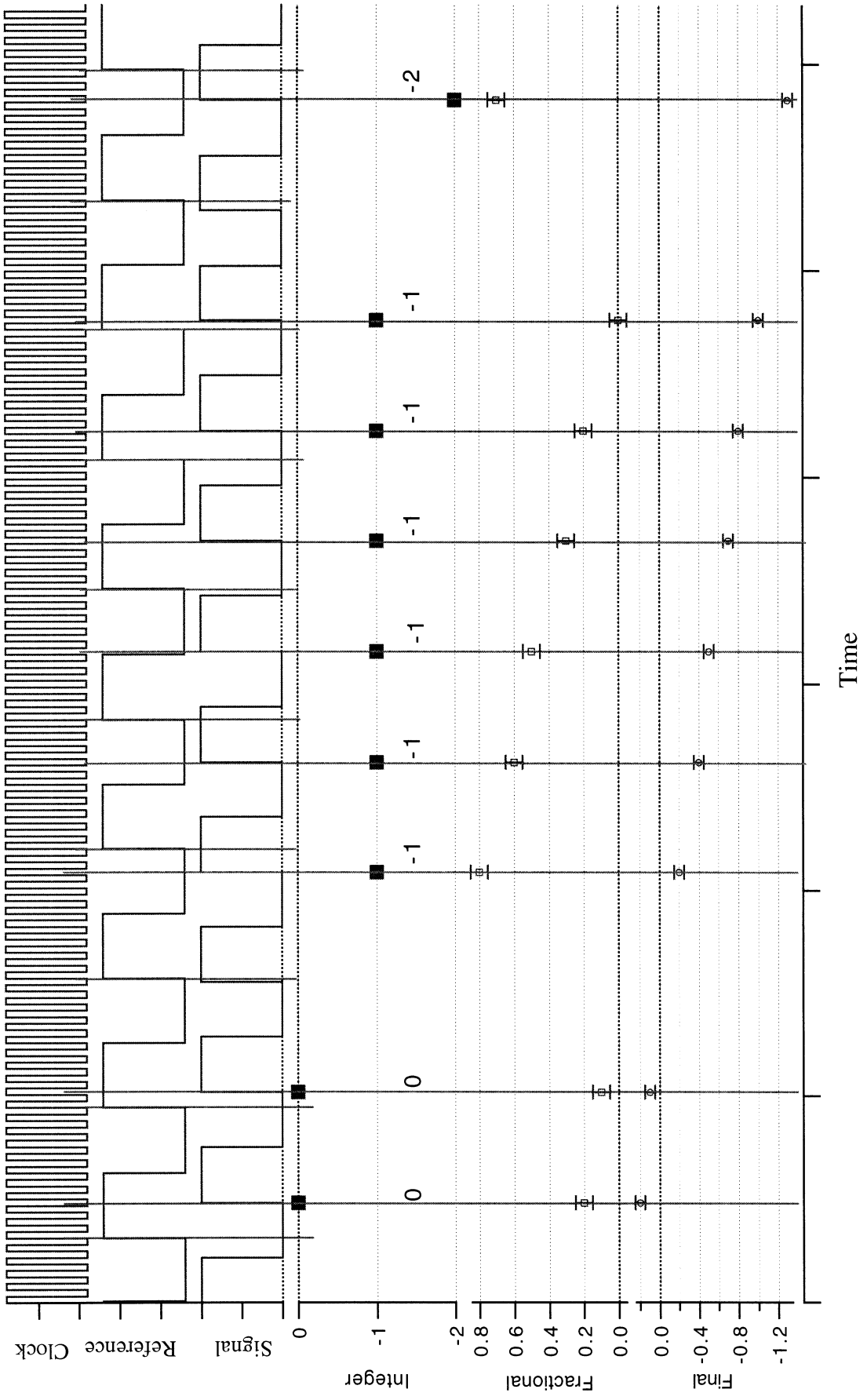
Clock
Reference
Signal
Integer
Fractional
Final
Time
0
-1
-2
0.8
0.6
0.4
0.2
0.0
-0.4
-0.8
-1.2

ANNEX B: Schematic set-up of the phase detection unit